Supplement of Solid Earth, 17, 407–427, 2026
https://doi.org/10.5194/se-17-407-2026-supplement

Solid Earth Open Access EGU

Supplement of

Feldspar alteration by disequilibrium CO_2-H_2O fluids in reservoir sandstones: implications for CCS

Natalie J. C. Farrell et al.

Correspondence to: Natalie J. C. Farrell (natalie.farrell@manchester.ac.uk)

S1. METHODS

S1.1. Experiment duration compared to geological timescales

Temperature exerts a strong influence on reaction rates, typically doubling the rate for every 10°C increase (Hall, 2015). Consequently, the six-day duration of our experimentally induced reactions corresponds to rates hundreds to thousands of times faster than those expected under reservoir conditions. To quantify this, we applied the Arrhenius equation to calculate reaction rate ratios and extrapolate the K-feldspar dissolution times observed in experiments conducted at 400°C and 550°C to the in situ reservoir temperature of 80°C. Calculations used two different activation energies for K-feldspar dissolution: 50 kJ/mol, reported by Blum and Stillings (1995) for dissolution in acidic conditions (pH ~3), and 38 kJ/mol, from Helgeson (1984) for dissolution under neutral pH conditions. Based on these activation energies, the K-feldspar dissolution observed at 400°C would translate to reaction times between approximately 7.7 and 53 years under reservoir conditions, indicating that the experiments proceed roughly 470 to 3300 times faster. Similarly, reactions observed at 550°C correspond to 26.6 to 274 years in situ, representing rates accelerated by factors of about 1600 to 16,000.

These calculations serve as a basic guide to assess the experimental results' relevance but do not account for additional rate-limiting or rate-enhancing factors, most notably the role of intergranular stresses in accelerating reaction rates. Nonetheless, these estimates suggest that the effects of K-feldspar dissolution could become significant within a CCS reservoir over human timescales.

S1.2. Experimental apparatus

Experiments were conducted using externally heated triaxial deformation apparatus, ‘Nimonic 2’ and ‘Nimonic 3’ (see main text for methodology).

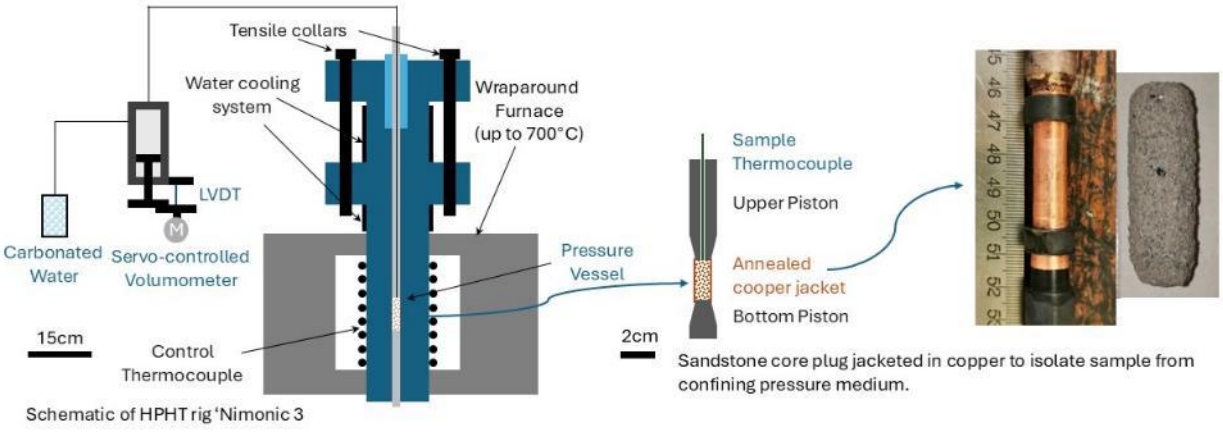

Figure S1. Schematic cross section diagram of high pressure, high temperature triaxial rig 'Nimonic 3' illustrating the sample assembly within the Nimonic pistons (rhs), confinement of sample with the pressure vessel and furnace (centre) and pore volumometer controlling injection and pressure of pore fluid along the top piston (lhs).

Tap water was used as the pore fluid for initial equilibration of the rock samples. This choice was intentional: rather than using deionised water, which is chemically undersaturated and can promote artificial mineral dissolution. The goal was to minimise the role of the water itself as a reactive agent during the saturation stage and better mimic natural formation fluids, which would typically be in partial equilibrium with the reservoir rock. By pre-equilibrating the water:rock system, we aimed to isolate and better assess the specific effects of CO_2-enriched fluids on mineral solubility and reactivity, rather than capturing reactions driven primarily by fluid disequilibrium.

Element	Symbol	Concentration (ppb)	Comparison to UK drinking water standards
Aluminium	Al	13	Below normal range
Iron	Fe	4.8	Very low
Zinc	Zn	21	Very low
Copper	Cu	6.7	Normal, very low
Lead	Pb	0.1	Normal very low
Arsenic	As	0.4	Very low
Calcium	Ca	4537	Normal, very low
Magnesium	Mg	1155	Below normal range
Sodium	Na	5792	Normal
Potassium	K	444	Below normal range

Table S1. Pore fluid chemistry of tap water used as pore fluid in reaction experiments analysed using ICP-MS

S1.3. XRD method

Measurements were carried out on a Bruker D2 Phaser diffractometer, equipped with a Lynxeye XE-T detector with an axial 2.5° Soller slit and anti-scatter screen. The X-ray generator was set to 30kV and 10mA, powering an X-ray tube with a copper source, providing $CuK_{\alpha 1}$ X-rays with a wavelength of 1.5406Å. Sample preparation involved grinding ~0.1g

sample material, mixed with ~1ml of amyl acetate, using a pestle and mortar. The resultant slurries were transferred to glass microscope slides and air dried.

Sample were scanned from 5-70º2θ, with a step size of 0.04 º and a count time of 0.4s per step. The resultant patterns were evaluated using EVA version 5, which compares experimental data to standards from the ICDD (International Centre for Diffraction Data) Database.

S1.4. Image analysis method

Pore and grain areas were quantified using the image analysis software ImageJ (Schneider et al., 2012). Image dimensions from the EDS/BSE datasets were imported into ImageJ, and a 10-pixel cutoff was applied to remove artefacts such as dust or metal particles introduced during polishing (Doyen, 1988). In BSE images, pores appear black and were therefore segmented using greyscale thresholding. Grain areas were extracted from coloured EDS images using colour-based thresholding. To account for heterogeneity and spatial distribution, the percentage area of each mineral was quantified from multiple subsections of each thin section (between six and twelve 3x3 mm images per sample).

In image-based analyses, the minimum detectable area (or volume) fraction is controlled by pixel size rather than an absolute percentage threshold, and can therefore be well below 1%, depending on image resolution. In this study, BSE images have a pixel resolution of 0.5 μm and EDS maps 1 μm, both of which are smaller than the practical uncertainty associated with image segmentation based on grey-scale or compositional thresholds. Edge effects (e.g. grain–pore transitions) introduce uncertainties on the order of 1 μm, while the effective sampled interaction volume for EDS is 3 μm, which we take as the relevant uncertainty scale.

The resulting uncertainty depends on grain size, perimeter length, and grain abundance within each segmented image. We therefore assess uncertainty by applying conservative and aggressive thresholding bounds (excluding versus including grain edges), with the range between these end-members representing the segmentation uncertainty. Applying multiple images across a poorly sorted sandstone section would tend to overestimate uncertainty due to large natural variability in grain size, abundance, and composition. Despite differences between segmentation approaches (e.g. ImageJ versus AZtec), the relative change between sections and experiments is consistent. We therefore have confidence that the reported decrease in volume fraction is robust. Data can be accessed at 10.6084/m9.figshare.31134949.

71

72 *S1.5. XCT image method*

73 X-ray CT images of pre- and post-experiment samples with voxel size of 3.37 µm3 were acquired on
74 a HeliScan™ micro-CT system at the Henry Moseley X-ray Imaging Facility at the University of
75 Manchester. The 3D images were processed and analysed using Avizo software (Thermo Fisher
76 Scientific). First, a sub-volume was extracted from the raw 3D data to exclude the image background,
77 reduce the impact of artefacts and improve computational efficiency. The non-local means and median
78 filters were then applied to the 3D images to reduce noise and enhance contrast between different
79 phases. These filtered 3D images were analysed to assess grain deformation in the post-experiment
80 samples. Although funding constraints prevented quantitative analysis of the datasets, the filtered 3D
81 images of the pre-experiment samples were segmented into two phases (solid and void) based on
82 greyscale intensity values, and used to generate simple pore network models. Images can be accessed
83 at 10.6084/m9.figshare.30061294.

84 S2. MATERIALS

85 Samples were collected from well 14/29a-5 at a range of depths from sandstone units defined as C, D
86 and E at depths listed in Figure 2.a and linked to wireline log data from the wellbore 2.b (Shell
87 Geochemical Reactivity Report, 2015). Mineral composition was determined for all samples using X-
88 ray diffraction analysis (Table 1).

a)

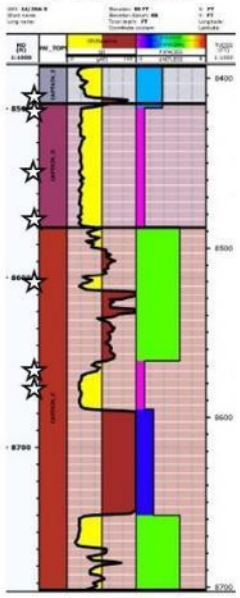

b)

Well	subunit	BGS sample	depth (ft)
14/29a- 5	E	SSK155547	8486.2
14/29a- 5	E	SSK155514	8486.1
14/29a- 5	top D	SSK155513	8500.5
14/29a- 5	top D	SSK155512	8500.6
14/29a- 5	middle D	SSK155510	8538.1
14/29a- 5	middle D	SSK155511	8538.6
14/29a- 5	Bottom D	SSK155509	8563.4
14/29a- 5	Bottom D	SSK155508	8563.5
14/29a- 5	top C	SSK155506	8601.5
14/29a- 5	top C	SSK155507	8601.6
14/29a- 5	middle C	SSK155505	8654.4
14/29a- 5	middle C	SSK155504	8654.5
14/29a- 5	middle C	SSK155503	8660.4
14/29a- 5	middle C	SSK155502	8660.5

c)

Figure S2. Sampling locations from well core. At each sample site 20mm diameter cores were plugged for provenance and images analysis and at 'D sand middle' and 'D sand top' 10 mm diameter cores were plugged for experiments (c).

	Wt% Rietveld						
Minerals	**C sand' massive**	**C sand' laminated**	**C sand' cemented**	**D sand' base**	**D sand' middle**	**D sand' top**	**E sand'**
Albite	7.6	10.3	0.2	2.4	8.1	6.4	4.6
Glauconite	0.1	0.8	0.7	1.1	1.1	0.0	0.2
Calcite	1.0	1.1	0.7	0.4	0.7	0.3	1.1
Kaolinite	4.0	9.0	3.1	0.5	7.7	5.8	8.0
Microcline	7.0	9.1	6.7	7.0	8.7	3.8	5.1
Quartz	80.3	69.6	86.7	88.6	73.0	83.6	81.0
Halite					0.8		
Augite Px			2.0				

Table S2. Mineral composition for all Captain Sandstone Formation sandstone units derived from XRD analysis.

Due to limitation on the amount of rock that could be sampled we used core plugs from the middle and top of the D sand unit in experiments. Sample mineralogy from 'D middle' comprised 73% quartz, **8.1% plagioclase, 8.7% K-feldspar, 7.7% kaolinite,** 1.1% glauconite, 0.7% calcite, 0.8% halite. Sample mineralogy from 'D top' contained 83.6% quartz, **6.4% plagioclase, 3.8% K-feldspar, 5.8% kaolinite**, 0.35% calcite (Table 1). Microstructural analysis of D middle and D top showed the D middle had more pore area 39% compared to D top 24.4% possible indicating higher porosities in the D middle samples.

S3. MICROSTRUCTURAL IMAGES

The following images show additional examples of mineral textures from BSE images (see main text for methodology) of pre experiment samples (Figure 3- 4) and post experiment samples (Figures 3-12)

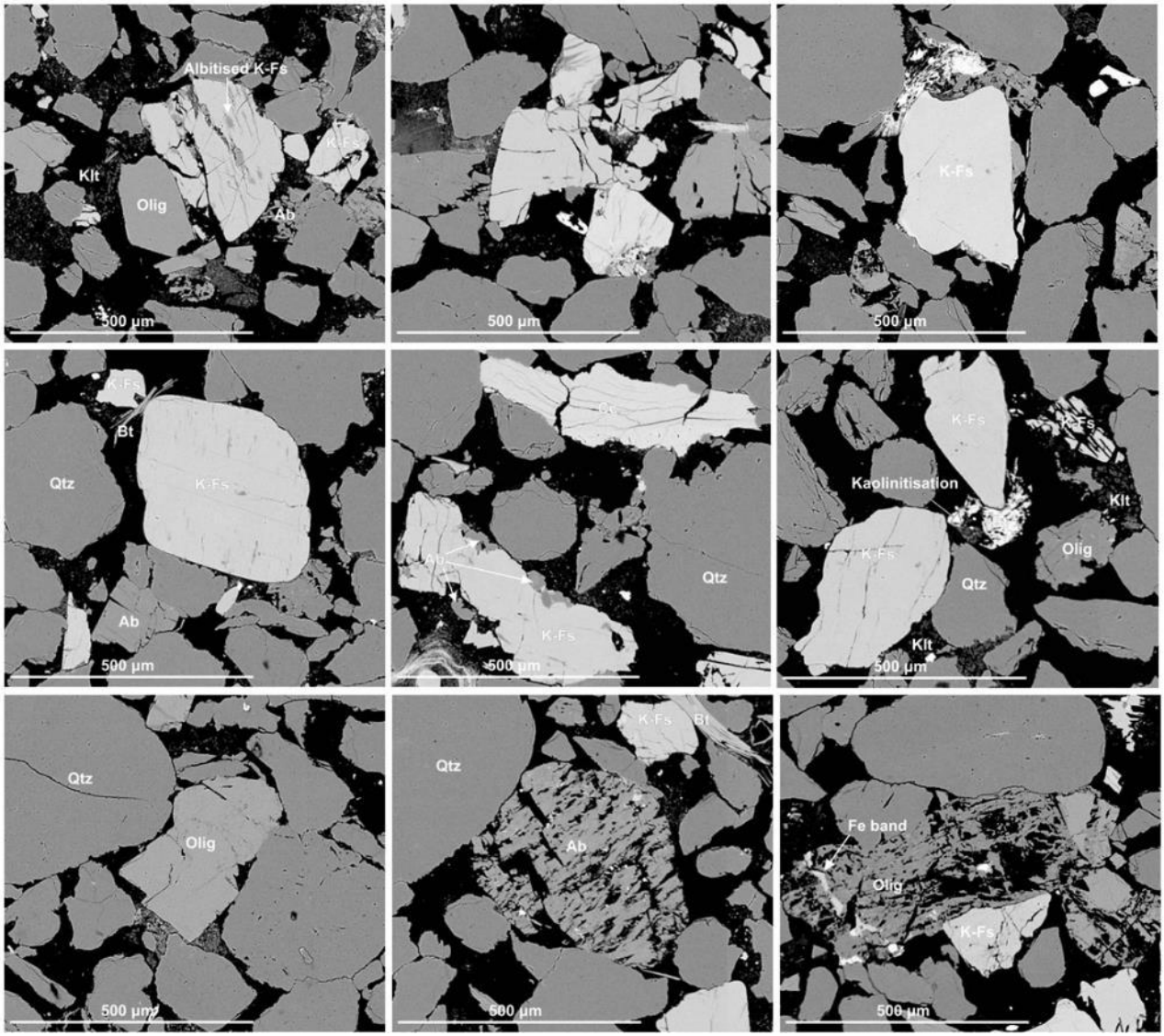

Figure S3. BSE images of feldspars in pre-experiment sandstone. Textures include pre-reaction K-feldspars with albitised lamellae and randomly oriented, curvilinear intergranular fractures related to crushing. Also shown are blocky, intact oligoclase grains and large skeletal albite grains with coherent grain boundaries. Abbreviations follow Whitney and Evans (2010).

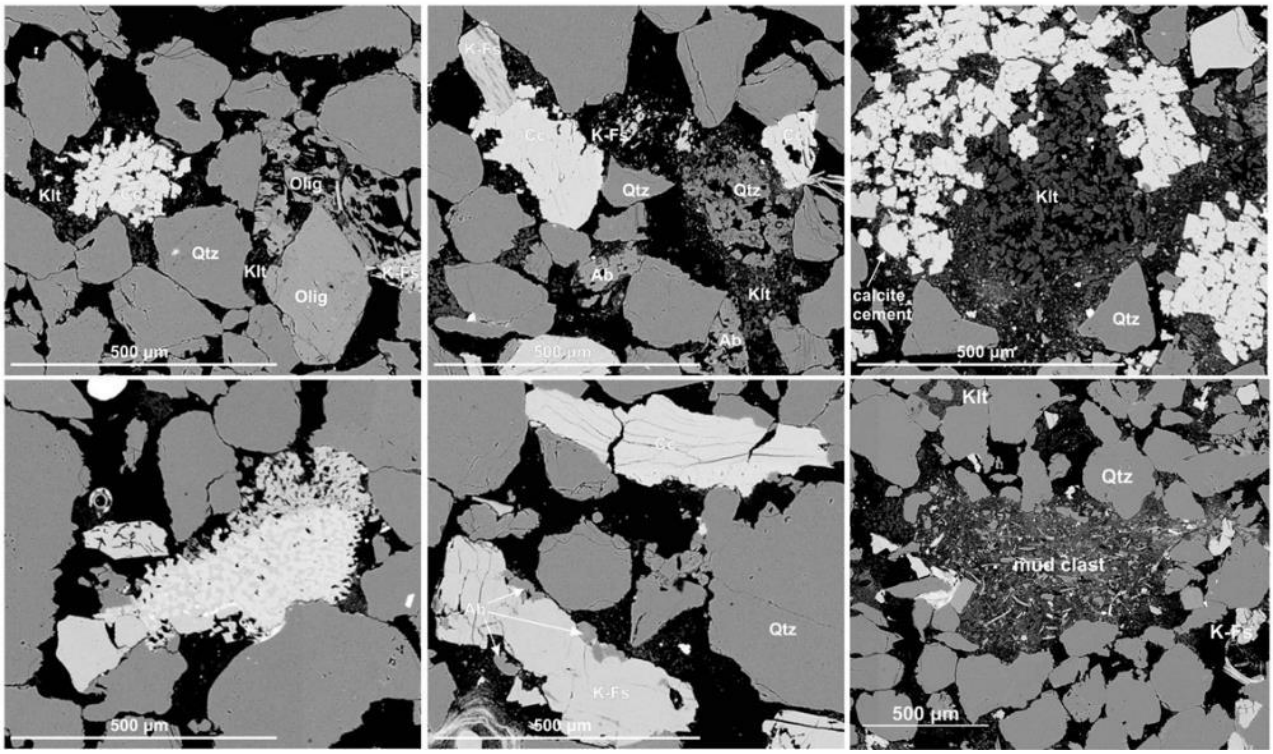

Fig S4. BSE images of calcite patches, grains, and clays in pre-experiment D sands. Features include patchy calcite associated with well-formed kaolinite patches and mud clasts containing mixed 1:1 clays.

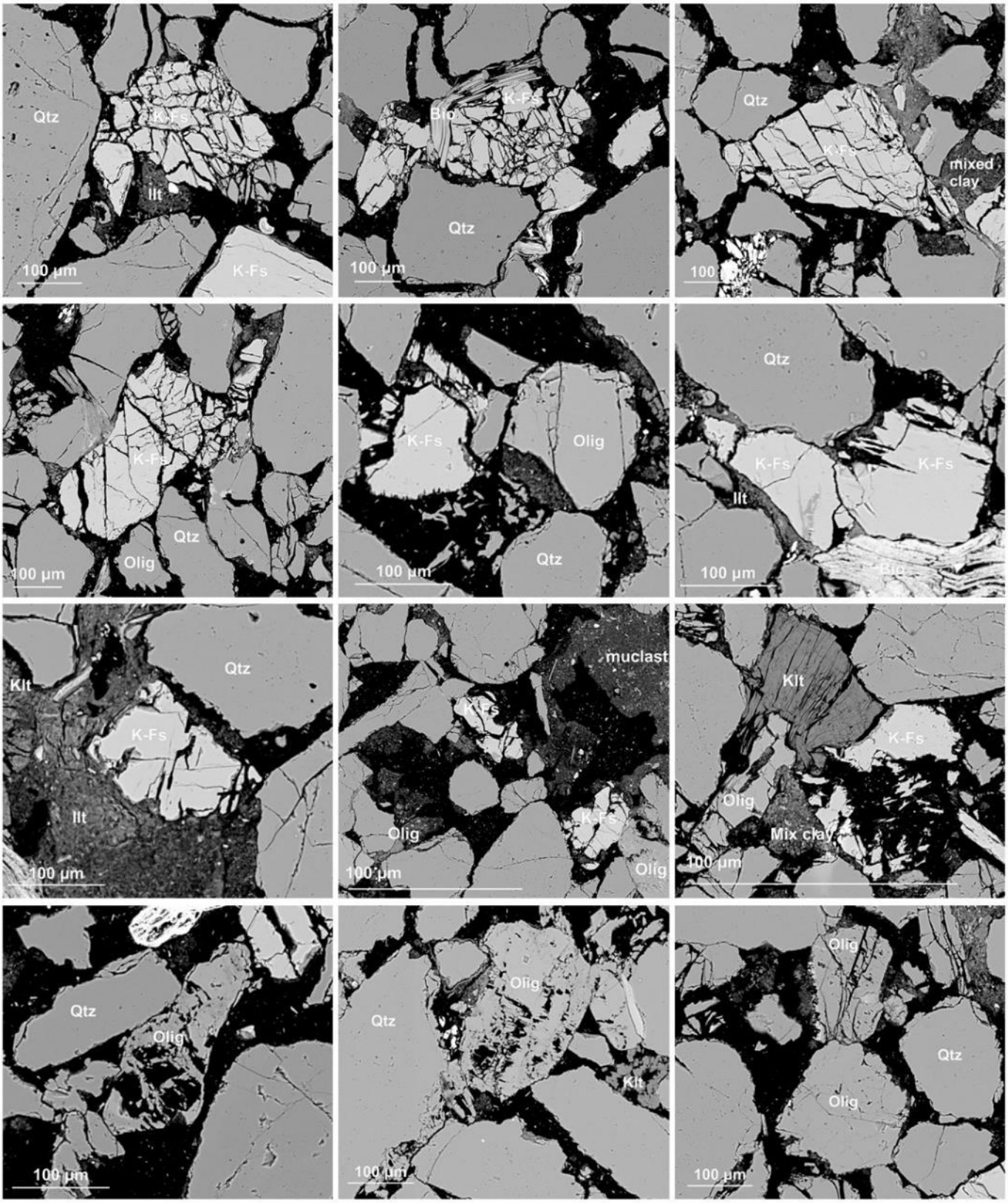

Figure S5. BSE images of sample Dt02, reacted with CO_2 fluids at 80°C. Larger K-feldspar (K-Fs) grains display fractures along semi-parallel intergranular fractures, likely reflecting structural weakening along cleavage planes, while smaller grains exhibit grain-edge cleavage cracks and partial dissolution. Secondary pores are commonly contain partially dissolved K-feldspar and some precipitates including illite (Ilt).

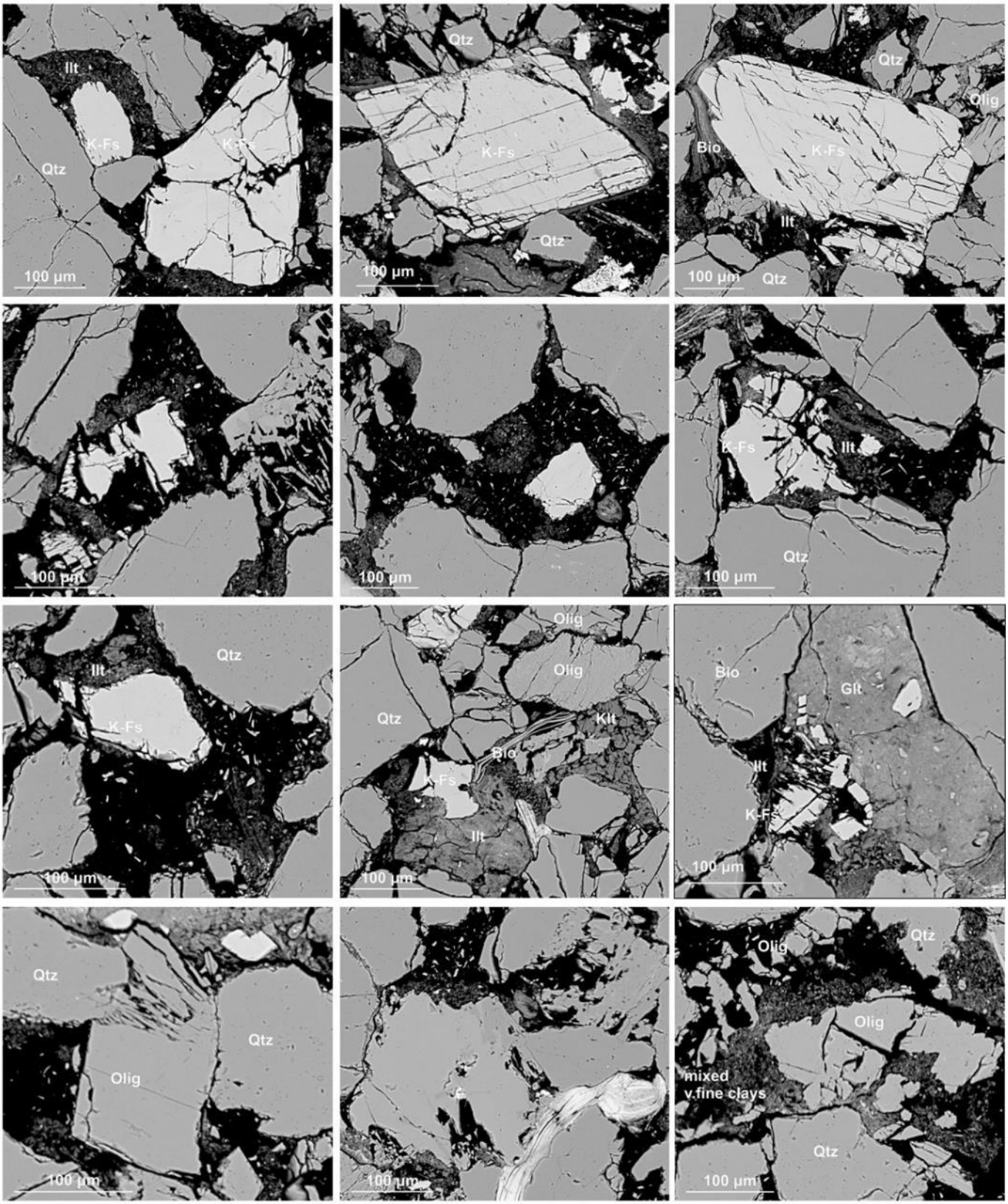

Fig S6. BSE images of sample DT01 reacted with CO_2 fluids at 250°C. Many K-feldspar (K-Fs) grains show dissolution along intergranular and grain-edge cleavage fractures. Secondary pores are commonly observed containing partially dissolved K-feldspar grains and illite (Ilt).

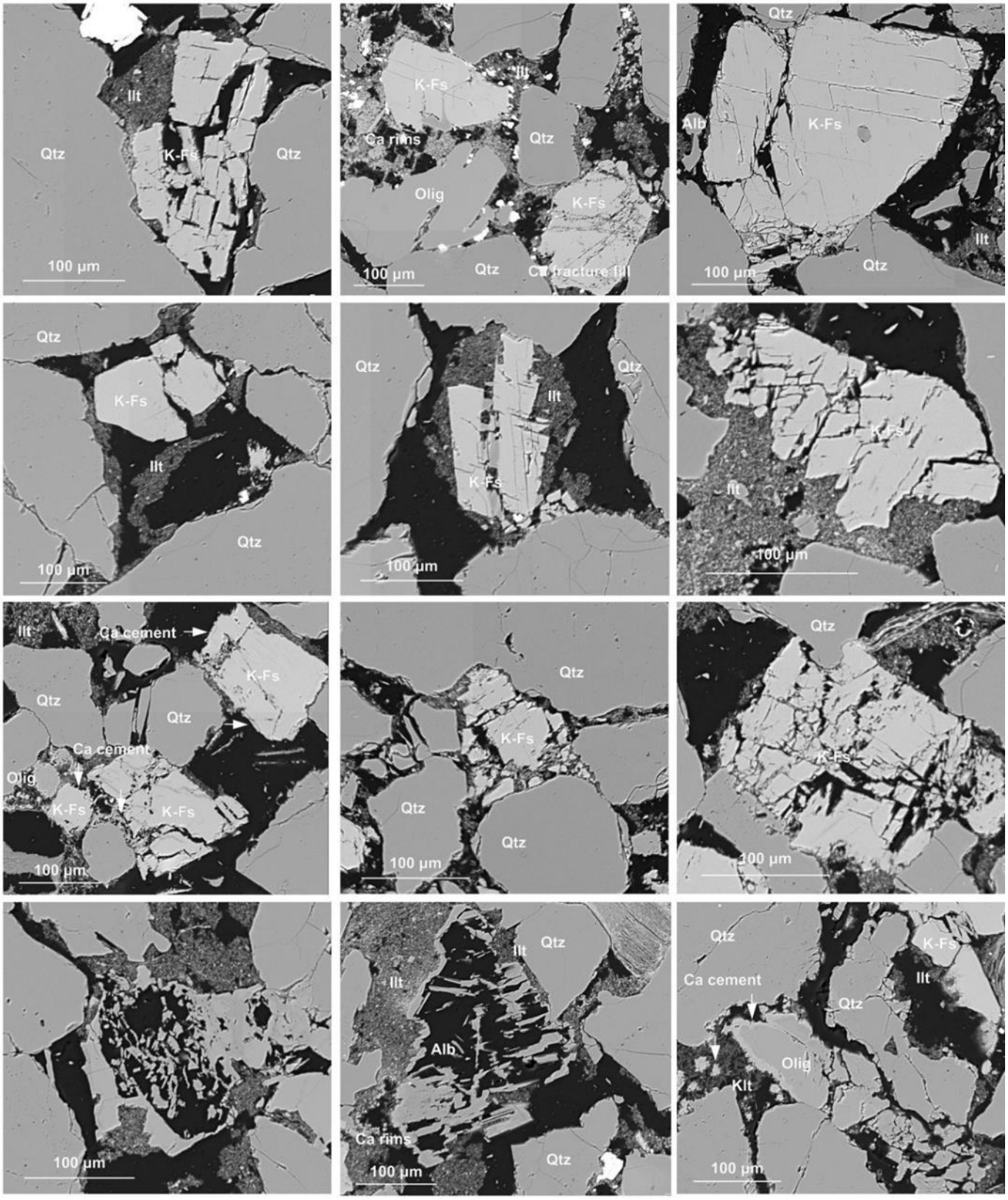

Fig S7. BSE images of sample DT03 reacted with CO_2 fluids at 400°C.

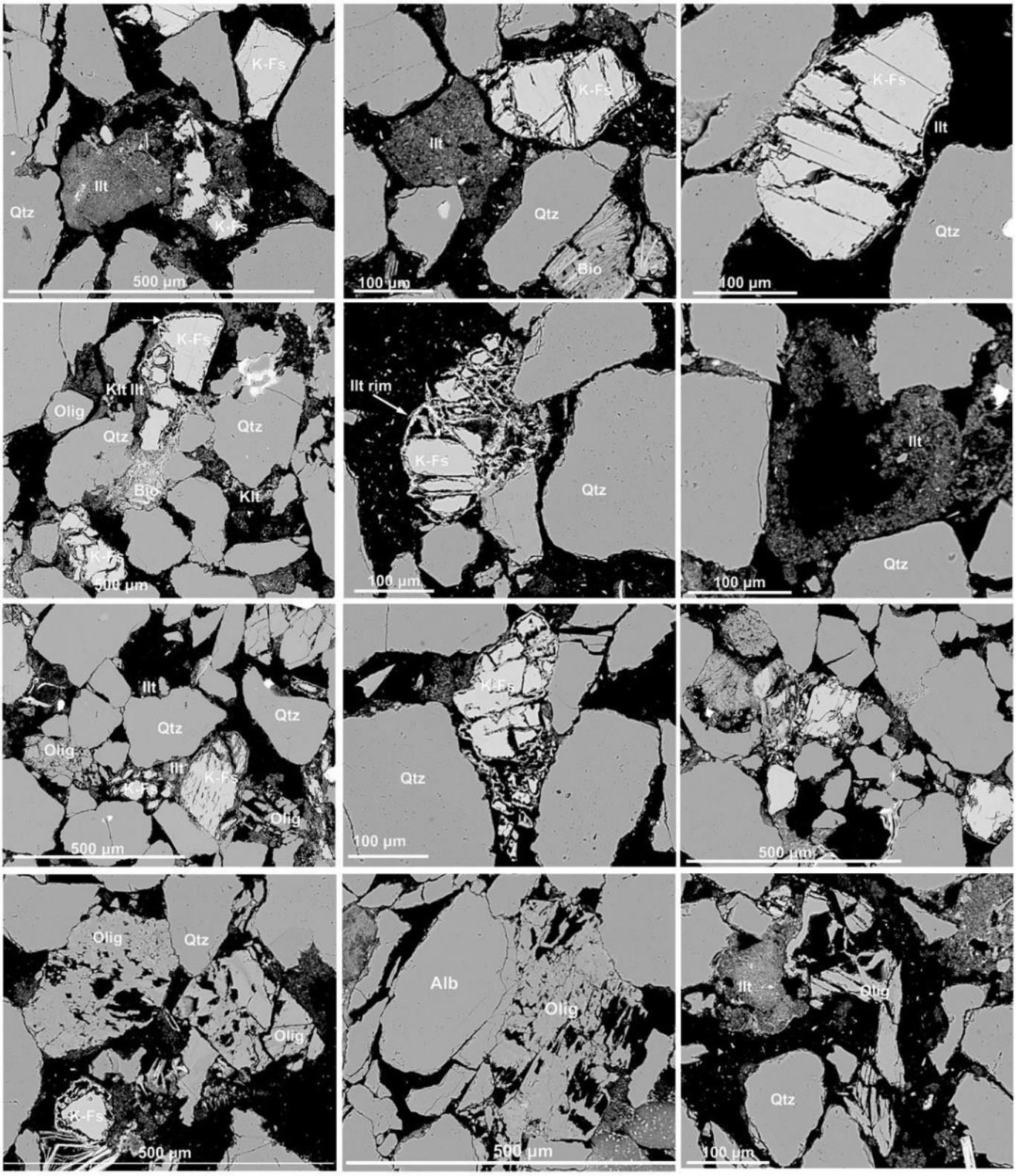

Fig S8. BSE images of sample DM05 reacted with CO_2 fluids at 550°C.

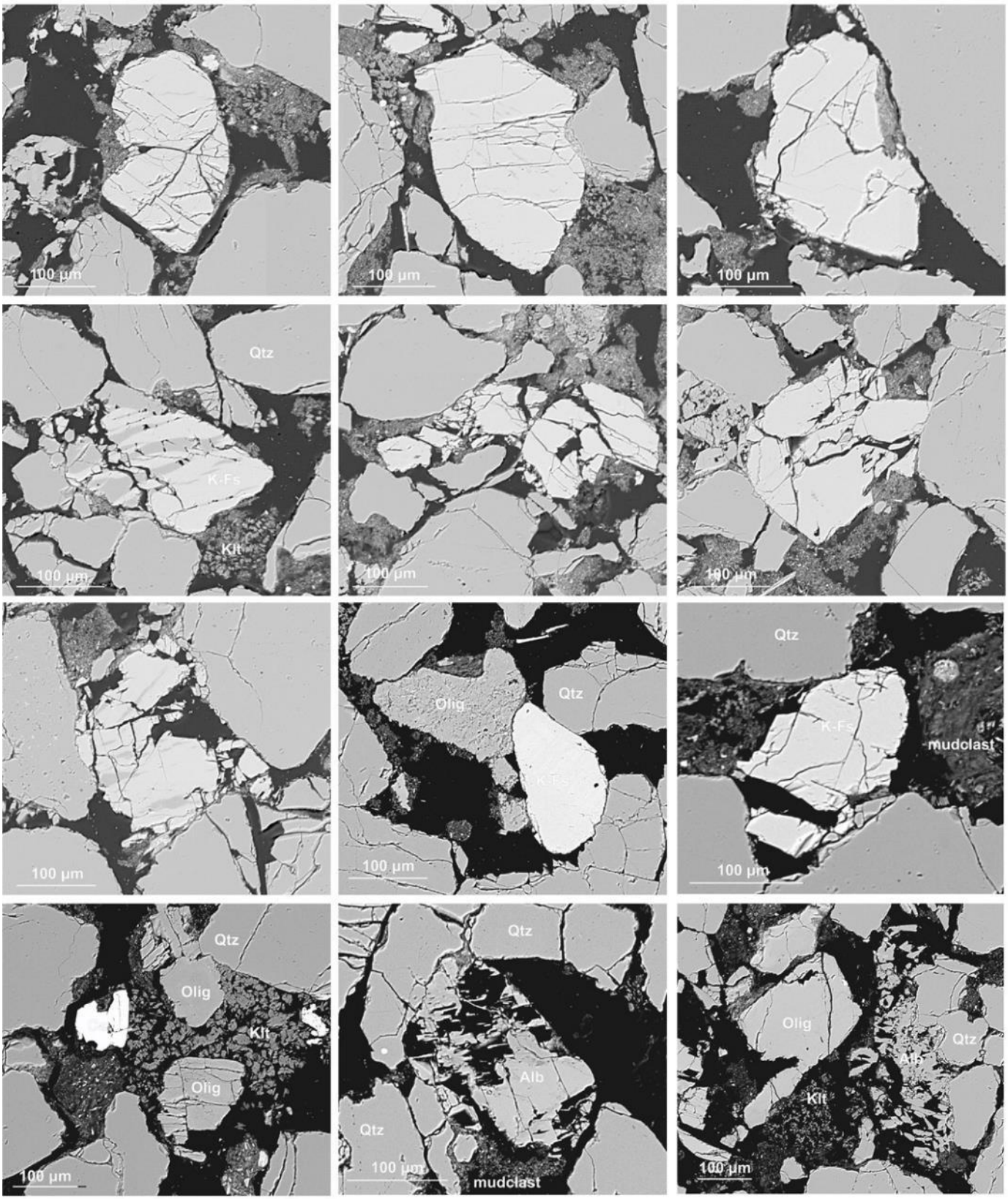

Fig S9. BSE images of sample Dm07 reacted with H_2O fluids at 80°C.

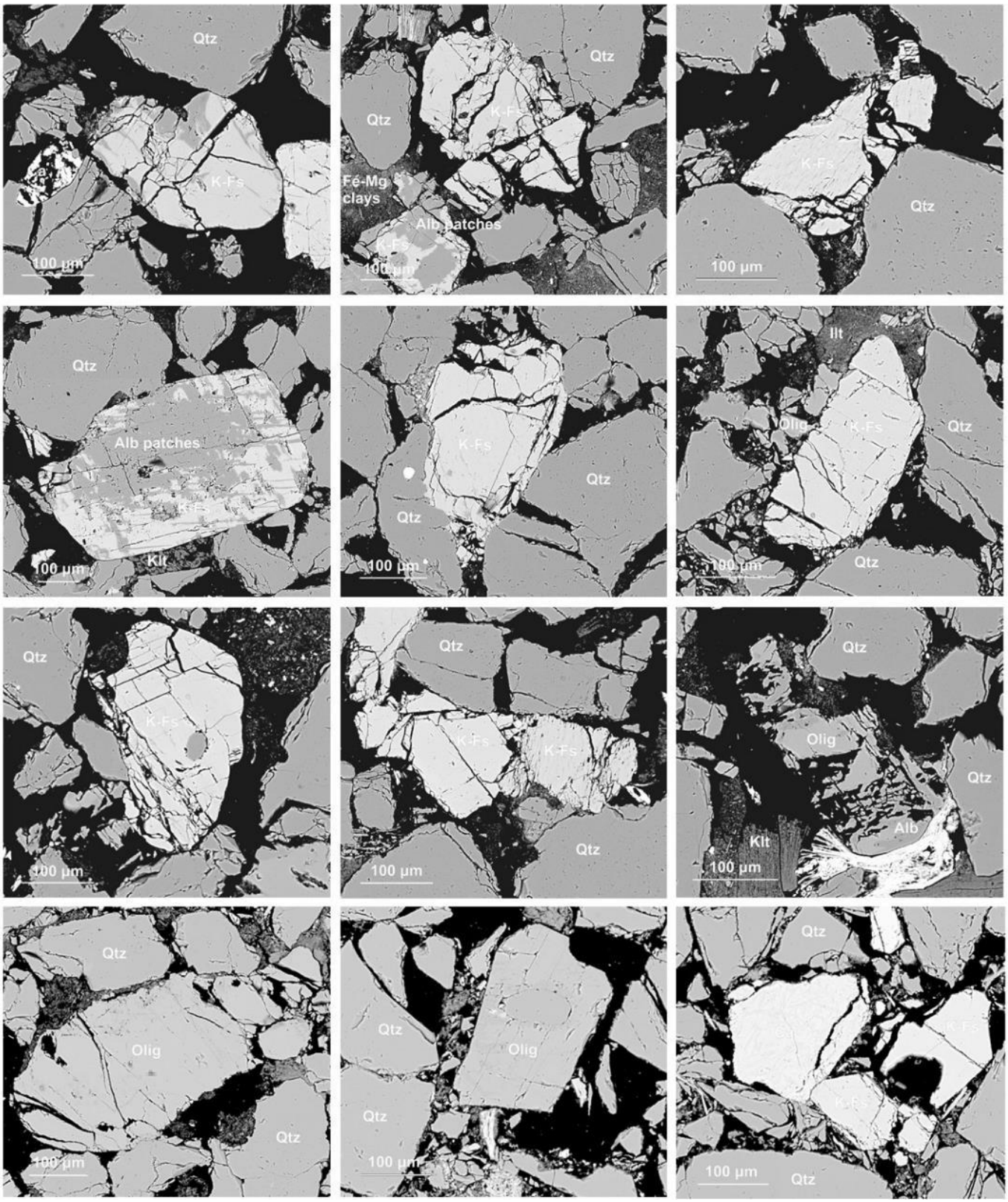

Fig S10. BSE images of sample Dm04 reacted with H_2O fluids at 250°C.

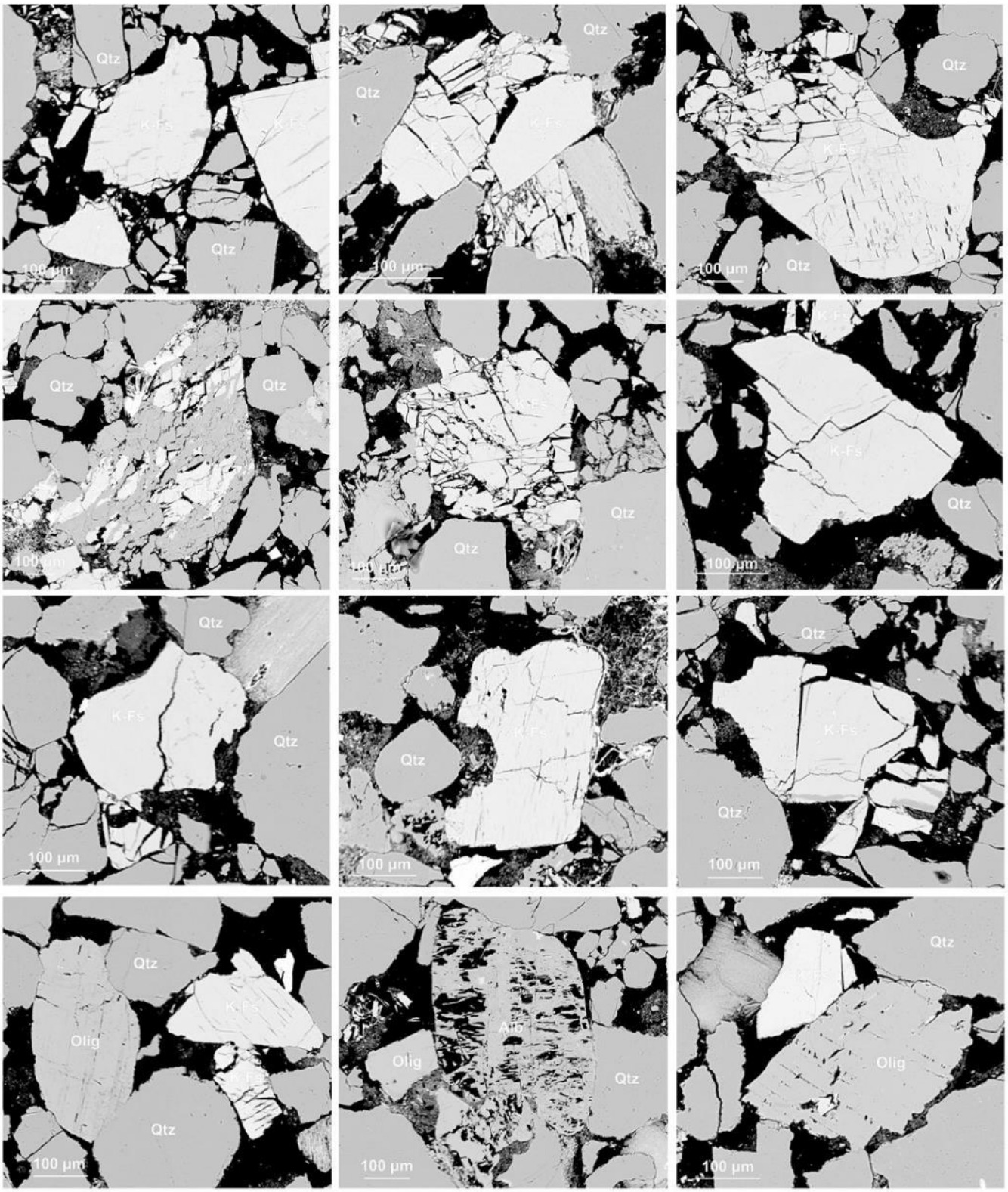

Fig S11. BSE images of sample Dm06 reacted with H_2O fluids at 400°C.

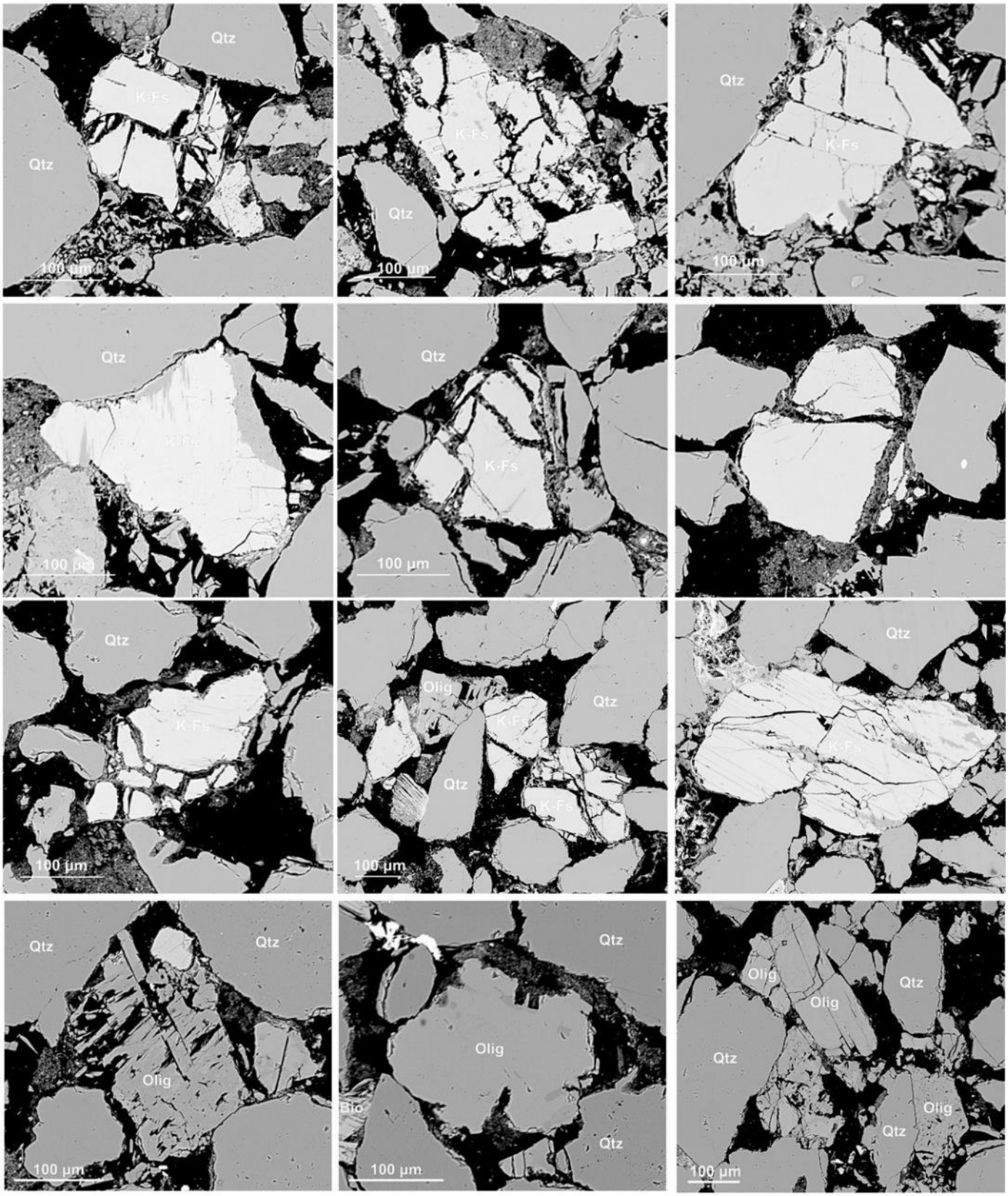

Fig S12. BSE images of sample Dm01 reacted with H_2O fluids at 550°C.

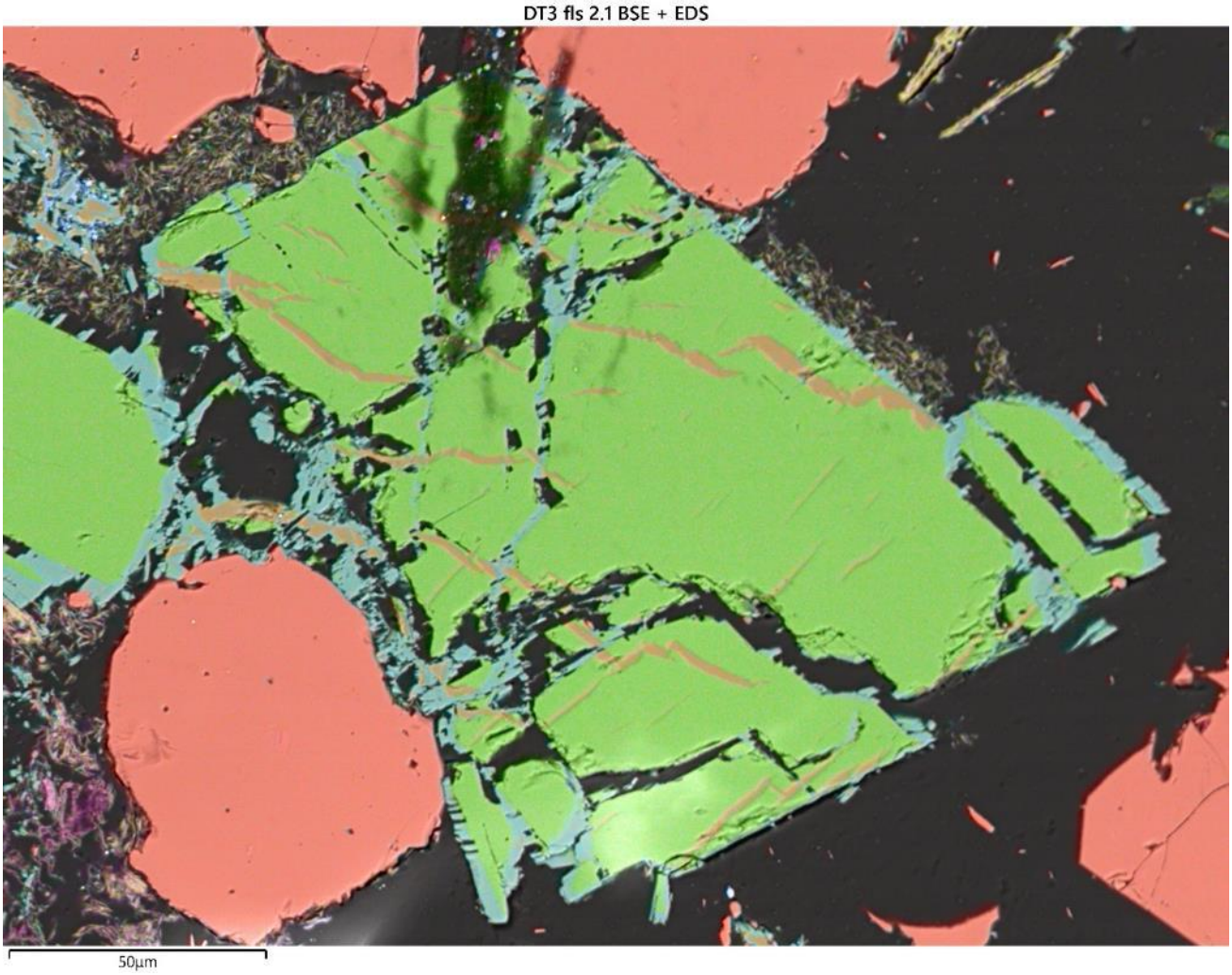

Fig S13. EDS BSE map of K-feldspar in post experimental sample DT03. In this image apparent anisotropic overgrowth of calcic aluminosilicates can be seen oriented from bottom left to top right of the image.

S4. FELDSPAR AND SECONDARY MINERAL COMPOSITIONS

Pre- and post-experimental feldspar compositions were determined using the SEM facility at CASP, as detailed in the main manuscript.

Pre-experimental compositions were extracted from a representative 7.5×7.5 mm representative large area map montages of the investigated DM and DT samples (https://doi.org/10.6084/m9.figshare.30084970.v2), using an accelerating voltage of 20 kV, a working distance of 8.5 mm, a probe current of approximately 2 nA and an EDS resolution of 1 µm. Using Oxford Instruments AZtec version 6.2, individual grains were traced to extract their composition and were calibrated using copper tape and Oxford Instruments "standardless" approach, as outlined by Pinard et al, (2020). A feldspar ternary plot (Fig 14) shows that the compositions are predominantly orthoclase, albite and oligoclase.

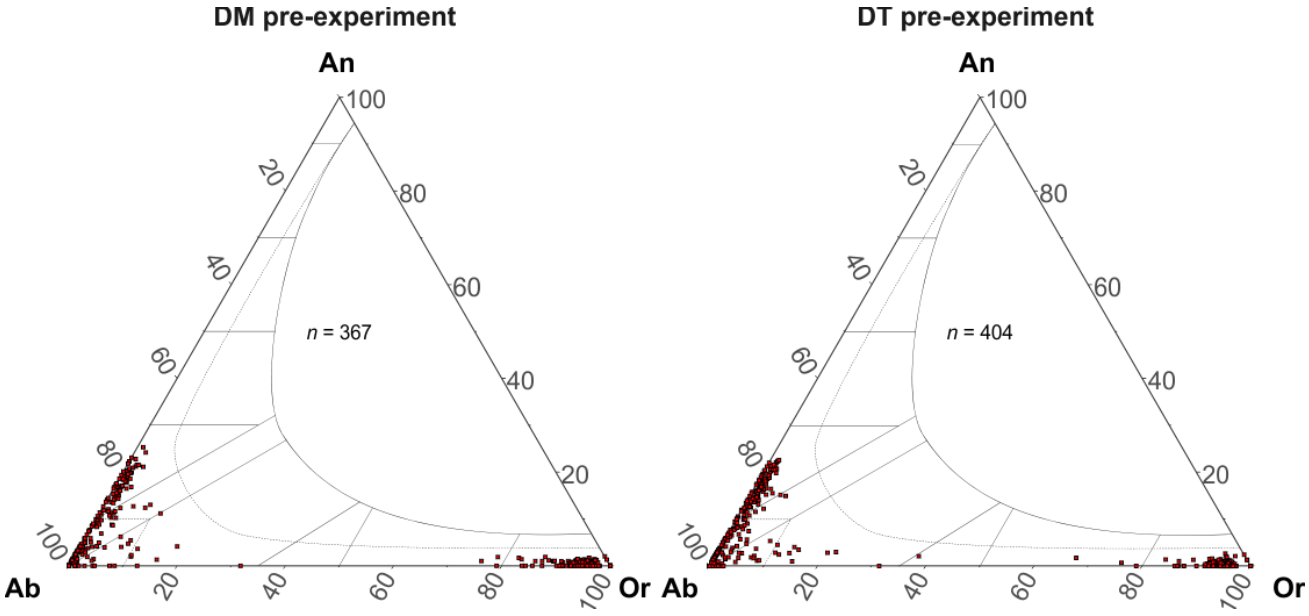

Figure S14. Ternary diagrams showing the composition of detrital feldspars for the pre-experimental DM and DT samples. Each point shows the average composition for a single detrital grain from a representative 7.5 mm^2 area.

Post-experimental analyses were determined using a spot analysis as follows: an accelerating voltage of 10 kV, a working distance of 8.5 mm and a probe current of approximately 2 nA. A mineral standard calibration was established using several phases in a MIN53-25 standard block (from Micro-Analysis Consultants Limited; Table 3), similar to the approach of Guyett et al. (2024). One million counts were collected per analysis by scanning over a rectangular area of <10 µm width at very high magnification. Beam intensity was calibrated using aluminium tape. Oxygen abundance was calculated from the stoichiometry. Labradorite from Tabor Island, Labrador, Canada, mounted in the MIN53-25 standard block was analysed intermittently as a secondary standard to confirm the veracity of the standard calibration and to monitor instrument drift (Table 4). The unnormalised sample data obtained are reported in excel file available at https://doi.org/10.6084/m9.figshare.30084970.v2 and the positions of spot analyses are shown on BSE images (Figure 15). The feldspar ternary plot of post experiment samples shows that the compositions are generally more calcic (Figure 16).

Element	Albite	Almandine	Diopside	Orthoclase	Benitoite	Celestine
O	48.78	40.33	43.72	46.72	34.51	35.03
Na	**8.51**		0.12	2.37		
Mg		3.46	**10.3**			
Al	10.54	11.47	0.38	**10.16**		
Si	31.93	17.48	25.16	**30.54**	19.8	
S						17.66
K	0.17			**9.83**		
Ca	0.07	1.11	**17.84**			
Ti			0.18		12.01	
Mn		0.93				
Fe		**25.21**	2.25			
Sr						**46.65**
Zr			0.06			
Ba				0.38	**33.67**	0.66

174 **Table S3. Materials analysed from the MIN53-25 standard to supplement the factory standard calibration for the**
175 **spot analyses. Elements shown in bold were used in the calibration of sample analyses.**

	Mean measured	2SE	Accepted average	2SE
O	47.32	0.15	47.18	0.03
Na	3.91	0.02	3.93	0.05
Al	14.85	0.05	14.87	0.05
Si	26.08	0.09	25.84	0.07
K	0.35	0.01	0.46	0.05
Ca	7.37	0.03	7.45	0.10
Fe	0.01	0.03	0.26	0.04

176 **Table S4. SEM-EDS chemical data from labradorite in standard block MIN-53-25. Based on 16 analyses. *Note**
177 **that Fe was not resolvable from the background for most of the analyses undertaken and is consequently**
178 **underrepresented and inaccurate. SE = standard error.**
179

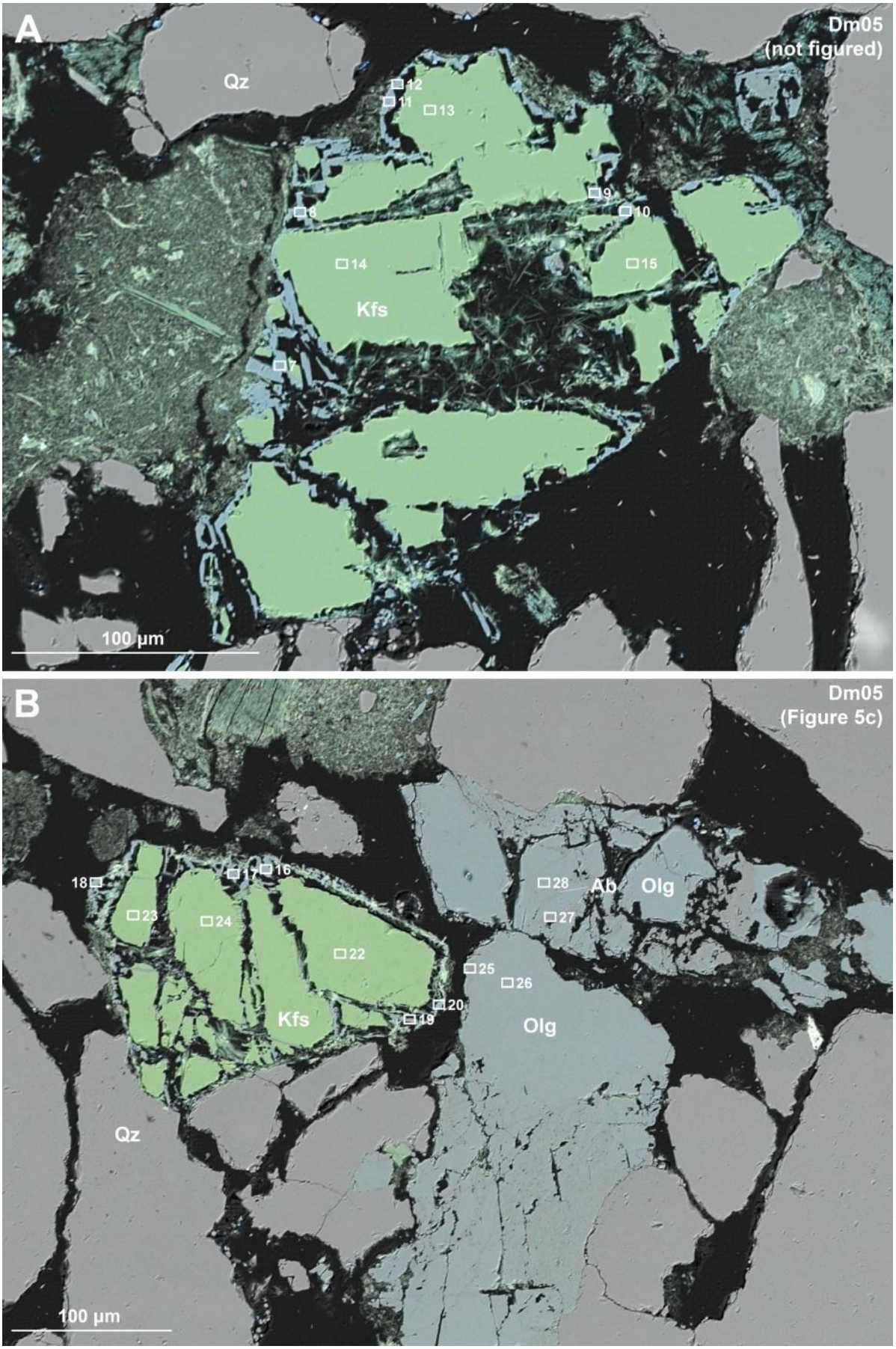
A
Dm05
(not figured)
Qz
12
11
13
9
10
6
14
15
Kfs
7
100 µm
B
Dm05
(Figure 5c)
18
17
16
28
Ab
Olg
23
24
27
22
25
26
20
Kfs
19
Olg
Qz
100 µm

180

Fig S15. Continued overleaf.

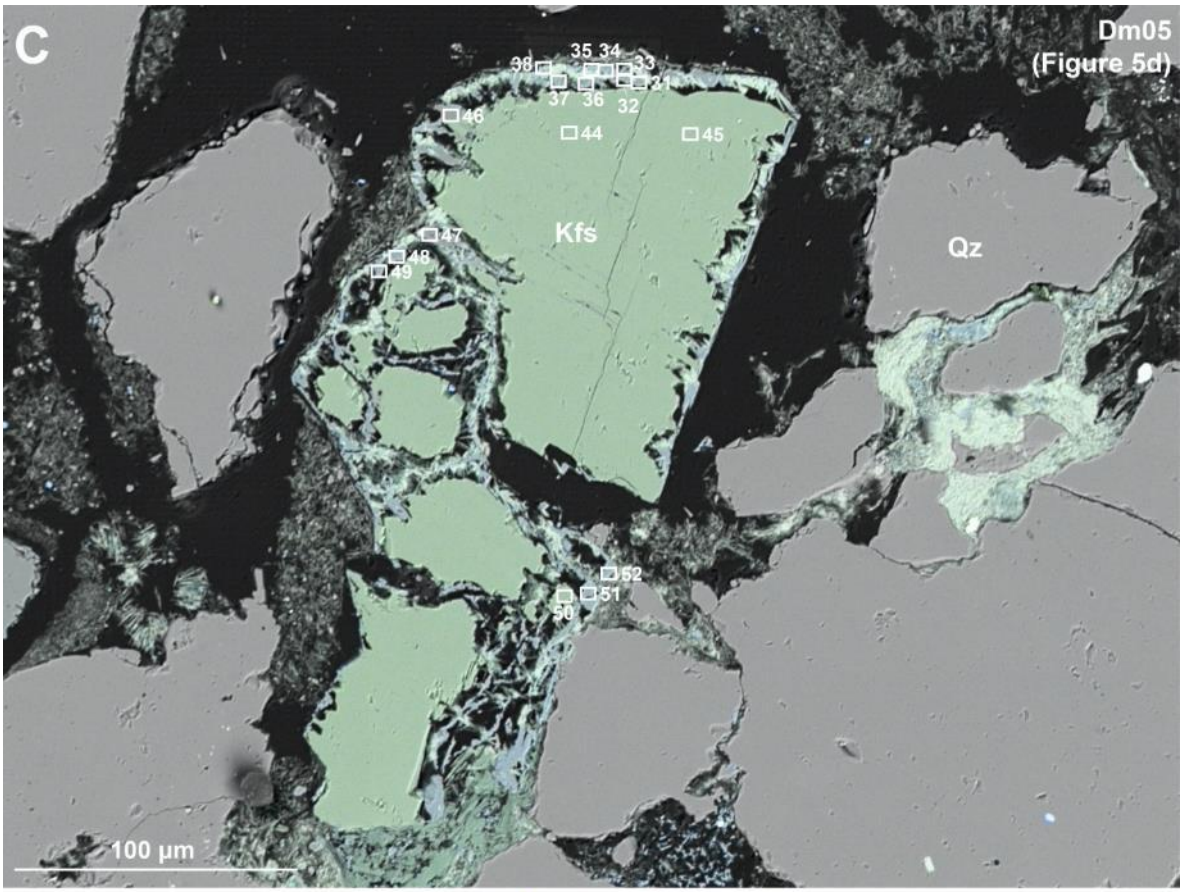

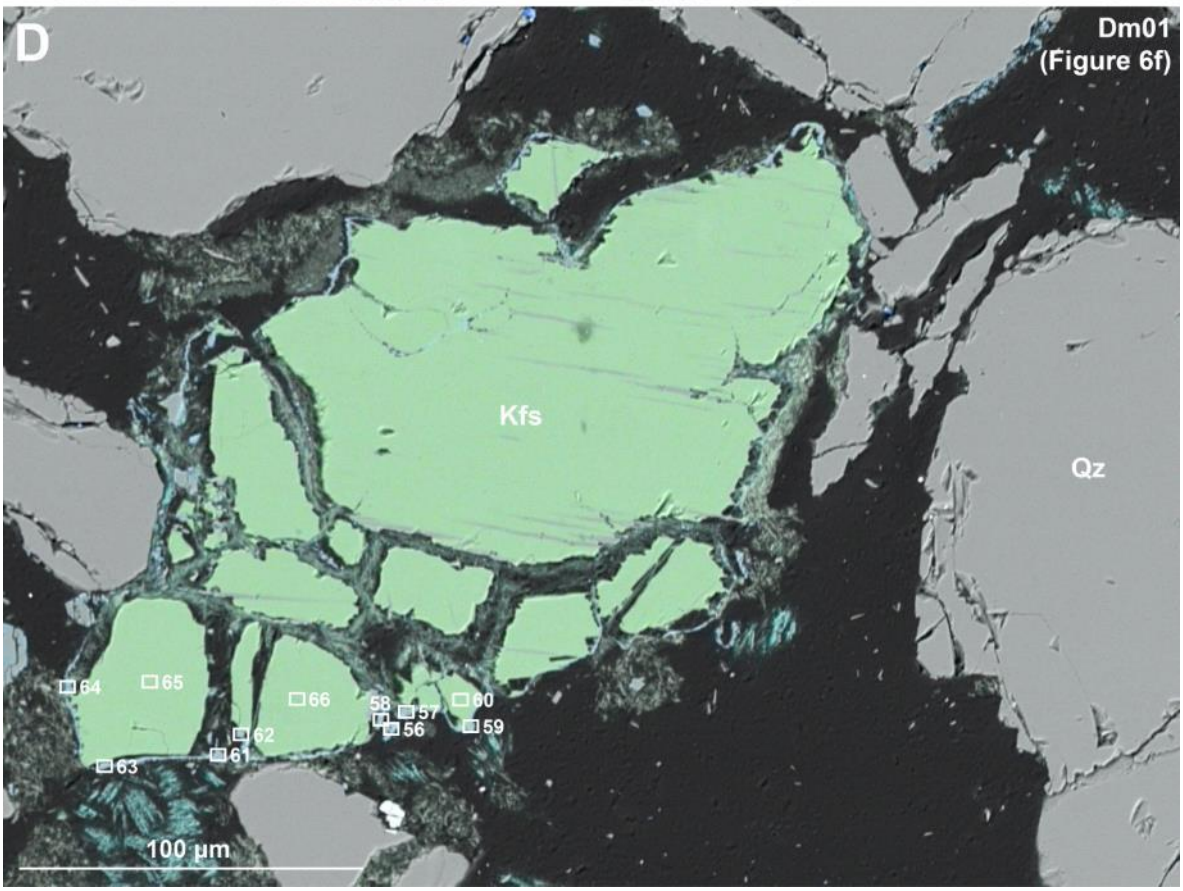

Fig S15. Continued overleaf.

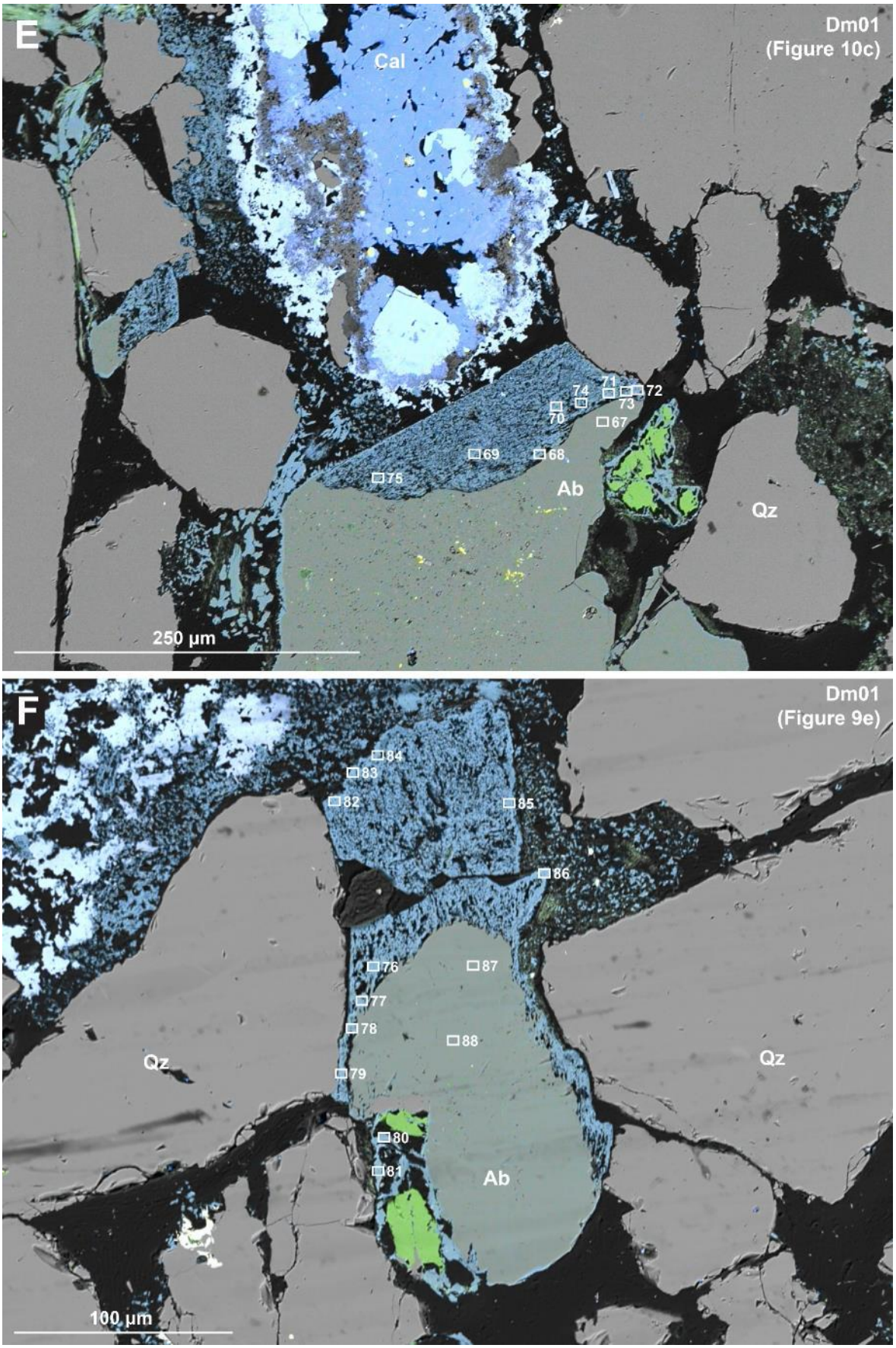

Fig S15. Continued overleaf.

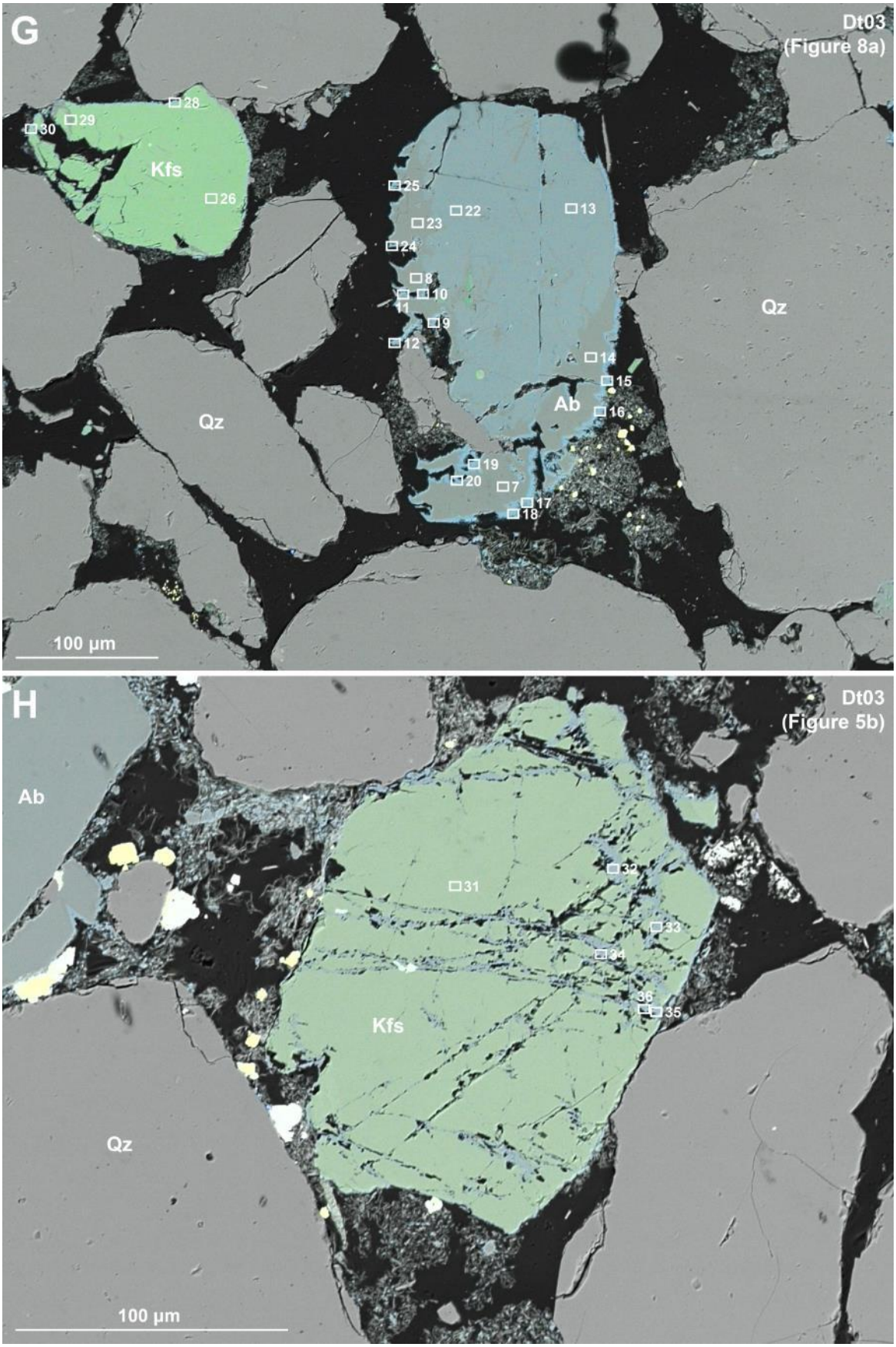

Fig S15. Continued overleaf.

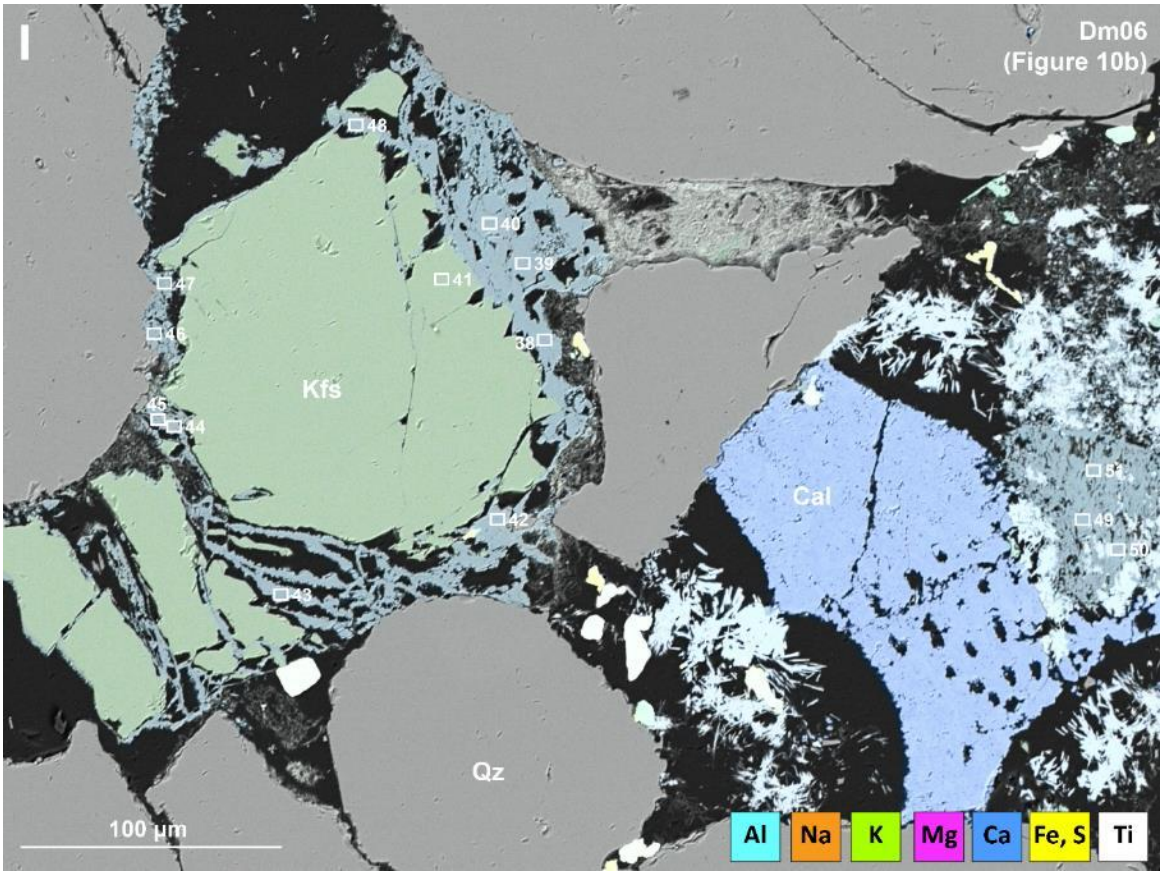

Fig S15. (A–I). BSE and semi-transparent EDS elemental maps showing the locations of feldspar spot analyses. All areas apart from A are figured in the main manuscript. The same elemental colours are used throughout.

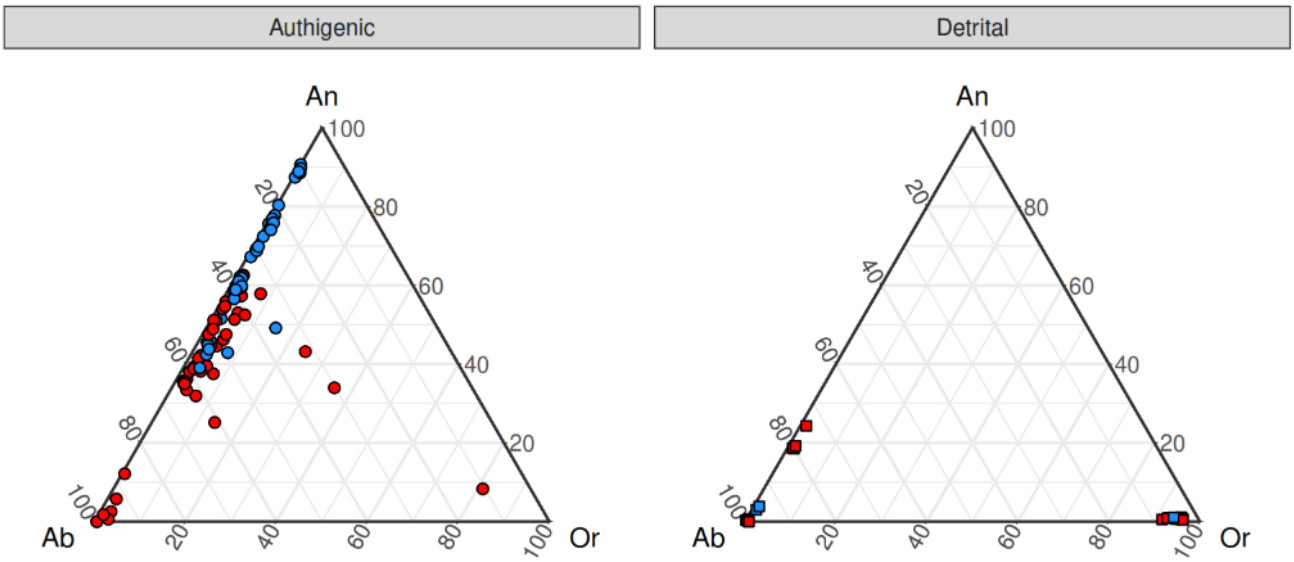

Figure S16. Ternary diagrams of feldspar compositions showing the new authigenic compositions and detrital grains, where red represents the CO_2 experiments and blue the H_2O experiments.

S5. References

Blum, A.E., Stilling, L. 1995. Feldspar dissolution kinetics. Chemical weathering rates of silicate minerals, pp.291-351.

Guyett, P.C., Chew, D., Azevedo, V., Blennerhassett, L.C., Rosca, C. and Tomlinson, E., 2024. Optimizing SEM-EDX for fast, high-quality and non-destructive elemental analysis of glass. Journal of Analytical Atomic Spectrometry, 39(10), pp.2565-2579.

Hall, M.R., Dim, P.E., Bateman, K., Rochelle, C.A. and Rigby, S.P., 2015. Post-CO2 injection alteration of pore network geometry and intrinsic permeability of Permo Triassic sandstone reservoir". Geofluids, 10.1111/gfl. 12146.

Helgeson, H.C., Murphy, W.M. and Aagaard, P., 1984. Thermodynamic and kinetic constraints on reaction rates among minerals and aqueous solutions. II. Rate constants, effective surface area, and the hydrolysis of feldspar. Geochimica et Cosmochimica Acta, 48(12), pp.2405-2432.

Pinard P.T., Protheroe A., Holland J., Burgess S. and Statham P.J. (2020) Development and validation of standardless and standards-based X-ray microanalysis. Materials Science and Engineering, 891, 012020.

Shell, 2015 'Peterhead CCS Project Doc Title: Geochemical Reactivity Report Doc No. PCCS-05-PT-ZR-3323-00001'. Available on Gov.UK website at PVT Modelling Report for CO2 in Goldeneye Project

214 Schneider, C.A., Rasband, W.S. and Eliceiri, K.W., 2012. NIH Image to ImageJ: 25 years of image
215 analysis. *Nature methods*, *9*(7), pp.671-675.

216 Whitney, D.L., Evans, B.W., 2010. Abbreviations for names of rock-forming minerals. Amer.
217 Mineral. 95, 185–187